Proceedings of the ASME 2019 14th International Manufacturing Science and Engineering Conference MSEC 2019 June 10-14, 2019, Erie, PA, USA

MSEC2019-3035

DESIGN RULES AND IN-SITU QUALITY MONITORING OF THIN-WALL FEATURES MADE USING LASER POWDER BED FUSION

Aniruddha Gaikwad*

Mechanical and Materials Engineering Department Lincoln, Nebraska, United States

Prahalada Rao

Mechanical and Materials Engineering Department Lincoln, Nebraska, United States

Farhad Imani

Industrial and Manufacturing Engineering, Pennsylvania State University, State College, United States

Hui Yang

Industrial and Manufacturing Engineering,
Pennsylvania State University, State College, United
States

Edward Reutzel

Applied Research Laboratory, Pennsylvania State University, State College, Pennsylvania, United States

Abstract. The goal of this work is to quantify the link between the design features (geometry), in-situ process sensor signatures, and build quality of parts made using laser powder bed fusion (LPBF) additive manufacturing (AM) process. This knowledge is critical for establishing design rules for AM parts, and to detecting impending build failures using in-process sensor data. As a step towards this goal, the objectives of this work are two-fold:

- Quantify the effect of the geometry and orientation on the build quality of thin-wall features. To explain further, the geometry-related factor is the ratio of the length of a thin-wall (l) to its thickness (t) defined as the aspect ratio (length-to-thickness ratio, l/t), and the angular orientation (θ) of the part, which is defined as the angle of the part in the X-Y plane relative to the re-coater blade of the LPBF machine.
- 2) Assess the thin-wall build quality by analyzing images of the part obtained at each layer from an in-situ optical camera using a convolutional neural network.

To realize these objectives, we designed a test part with a set of thin-wall features (fins) with varying aspect ratio from Titanium alloy (Ti-6Al-4V) material – the aspect ratio l/t of the thin-walls ranges from 36 to 183 (11 mm long (constant), and 0.06 mm to 0.3 mm in thickness). These thin-wall test parts were built under

three angular orientations of 0° , 60° , and 90° . Further, the parts were examined offline using X-ray computed tomography (XCT). Through the offline XCT data, the build quality of the thin-wall features in terms of their geometric integrity is quantified as a function of the aspect ratio and orientation angle, which suggests a set of design guidelines for building thin-wall structures with LPBF. To monitor the quality of the thin-wall, inprocess images of the top surface of the powder bed were acquired at each layer during the build process. The optical images are correlated with the post build quantitative measurements of the thin-wall through a deep learning convolutional neural network (CNN). The statistical correlation (Pearson coefficient, ρ) between the offline XCT measured thin-wall quality, and CNN predicted measurement ranges from 80% to 98%. Consequently, the impending poor quality of a thin-wall is captured from in-situ process data.

Keywords. Additive manufacturing (AM), laser powder bed fusion (LPBF), in-process monitoring, quality assurance (QA), design rules, thin-wall features.

^{*} Corresponding author. Email: Tel.: +01-402-472-3458. E-mail address: aniruddha.gaikwad@huskers.unl.edu

1 Introduction

1.1 Background and Motivation.

The goal of this work is to understand the link between part design features (geometry), in-situ process sensor signatures, and build quality of parts made using laser powder bed fusion (LPBF) additive manufacturing (AM) process specifically focused on thin-wall features. In LPBF, Figure 1, a thin layer of powder is raked or rolled across a build plate, and subsequently, this layer of powder is selectively melted using energy supplied by a laser beam. The laser beam is typically focused on the powder bed through an f- θ lens, which maintains a flat field of projection irrespective of the angle incidence of the laser beam [1].

For most materials processed in LPBF, the power of the laser beam is set in the range of 200 W to 500 W, the velocity with which it travels ranges from 500 mm/s and 1000 mm/s, and the contour and hatching parameters are typically different. After a layer is selectively melted, the build plate is lowered by a distance typically in the range of 50 µm to 100 µm, and another layer is deposited [2, 3]. This process continues until the part is built. In LPBF, there are complex intertwined relationships between part design, process parameters, thermal phenomena, resulting in heterogeneity in part microstructure mechanical properties [2].

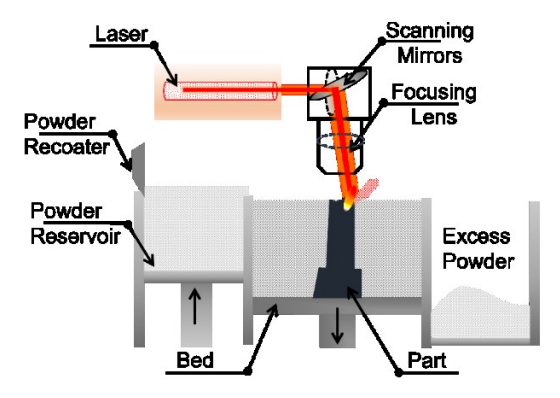


Figure 1: Representation of the laser-based powder fusion process [4].

This work concerns with the fabrication of thin-wall structures using LPBF. Thin-wall structures are extensively used in industrial applications, for a variety of reasons, such as to reduce the weight of a component without compromising its structural integrity. Figure 2 shows a titanium spinal implant consisting of thin-wall structures. The manufacture of such intricate geometry, which is difficult, or impossible, to make with conventional subtractive and formative manufacturing process, is made possible through LPBF [5-7]. However, the process anomalies in LPBF, and the inherent geometry of thin-wall structures makes the AM build highly susceptible to failure (e.g., collapse, superelevation, porosity, poor structural quality) [8-10]. In this work, defects in these thin-walls are analyzed in order to propose quantitative design rules, and to develop an in-situ monitoring

system to assess thin-wall quality. To investigate these factors, representative build defects observed in a test artifact with thin-wall features are shown in Figure 3.

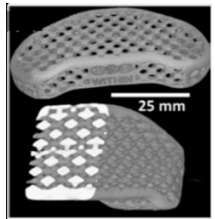


Figure 2: X-Ray computed tomography (XCT) scan of a titanium spinal implant consisting of thin-wall structures.

The geometric integrity of the thin-wall can be affected by the restricted heat flux due to their smaller cross-section area. The restricted heat flux leads to sharp thermal gradients, which in turn may cause cracking and warping (distortion) defects [11, 12]. Another common reason for the frequent failure of thinwalls is the interaction of thermal and mechanical factors; the geometric distortion of the thin-wall due to the thermal gradients causes the part to protrude out of the powder bed, a phenomenon called super-elevation, which leads to contact of the part with the re-coater [13, 14]. The contact of the part with the re-coater is liable to damage the re-coater (re-coater jam or crash), and the thin-wall features may fail as they are ill-disposed to resist the transverse force exerted by the re-coater. Given these risks, there is a compelling need to provide design rules for hard-to-build features, such as thin-walls and overhang geometries, so that extensive process optimization is precluded. Within the same context, it is critical to detect imminent build failures, to implement opportune corrective actions [15, 16].

1.2 Objectives.

In the context of the aforementioned scientific rationale concerning design rules and process monitoring in AM, the objectives of this work are as follows.

- Formulate geometric design rules for the manufacture thinwall parts made using the LPBF process. These design rules take the following form: given a build orientation and height of a thin-wall feature, what should be its thickness. Alternatively stated, given the length and thickness of a thinwall, what should be the maximum allowable build height, and corresponding build orientation.
- 2) Detect the onset of build failures in thin-wall parts using data from in-situ process sensors.

To achieve the first objective, we designed a test artifact having thin-wall features with varying dimensions. A schematic of the thin-wall test part is shown in Figure 5. The details of the test artifact are discussed in Section 3.1. Three such test parts were built, each differing in its angular orientation (θ) to the direction of the re-coater blade. Subsequently, we examine each of the thin-wall builds using X-ray computed tomography (XCT) (e.g. Figure 3(b)). The build quality of the thin-wall is quantified using features extracted from layer-wise XCT slices with the

help of image processing algorithms. These features are tracked across layers, and are thereafter used as derived features of thinwalls. Geometric design rules for thin-wall features are proposed based on these empirical quantitative measures. We make the following clarification regarding the aspect ratio (l/t). The aspect ratio of a feature is taken to imply the ratio of its largest dimension to its smallest dimension. For instance, the aspect ratio of a circular hole is the ratio of its depth over diameter. Similarly, in the specific context of this work, the aspect ratio is the length (l, largest dimension) to the thickness (t, smallest dimension) of the thin-wall (Figure 3 (a)). The length of the thinwalls is held constant at 11 mm, whilst the thickness ranges from 0.06 mm to 0.3 mm. Another reason for defining the aspect ratio in the foregoing manner is that, in this work, the height of the thin-walls varies such that the height-to-thickness ratio is held constant at 10 (height and thickness of each thin-wall is reported in). Accordingly, one of the design rule proposed in this work is the maximum build height of a thin-wall given its aspect ratio (l/t) and orientation to the direction of the re-coater blade. To address the second objective, we developed an optical imaging setup that takes a picture of the surface of the powder bed after each layer is deposited. These images are further analyzed using a convolutional neural network (CNN), which is trained to predict the build quality features extracted from XCT images from the first objective. As a consequence, the part quality in terms of its geometric integrity can be tracked using the in-situ process data to pre-empt failure.

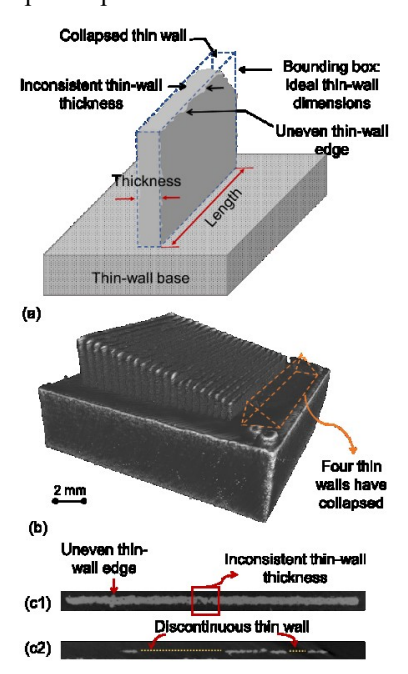


Figure 3: (a) Various defects that may occur in a thin-wall structure built using LPBF process. (b) XCT scan of a thin-wall part at 60° orientation angle. The thin-walls with aspect ratio of $55 \ (l/t, 11 \ \text{mm}/ 0.15 \ \text{mm})$ and $36 \ (l/t, 11 \ \text{mm}/ 0.1 \ \text{mm})$ are shown (c1) and (c2) respectively. These images depict the different defects in thin-wall structures.

1.3 Organization of the paper

The rest of this paper is organized as follows. A brief summary of the relevant design for AM is provided in section 2. This is followed by the description of experimental procedure in section 3, including a brief description of the thin-wall test artifact, and a procedure for data acquisition. Section 4 describes the methodology used for quantification of thin-wall build quality from XCT scan data, and the detailed analysis of the powder bed images using a deep learning convolutional neural network (CNN). The results from this work are discussed in Section 5, in which the design rules derived from the analysis of XCT scan slices are put forth, and the fidelity of the CNN in predicting the quality of the thin-wall is quantified. Finally, the conclusions stemming from this work, and avenues for future research are summarized in Section 6.

2 Literature Review

Powder bed fusion (PBF) additive manufacturing (AM) processes, despite their revolutionary potential, have intrinsic shortcomings, such as material constraints, surface finish, part accuracy and repeatability, and these factors have impeded its use in a production environment [17]. Furthermore, parts that are additively manufactured have particular distinguishing characteristics, such as intricate geometries, custom part design, low productions volume, and complex material compositions [18]. One of the main bottlenecks in AM are the absence of design guidelines that can be used as rules-of-thumb by practitioners to avoid poor quality parts [19]. It is therefore essential to propose design guidelines for AM. According to Rosen, design for additive manufacturing (DFAM) is defined as, "maximizing product performance through the synthesis of sizes, hierarchical structures, and material compositions, subject to the capabilities of AM technologies," [18].

The conventional design for manufacturing (DFM) rules do not apply for AM parts as they are manufactured layer-by-layer, and are bottom-up processes, unlike the conventional methods, such as machining, which is top- down. Hence, the unique layer-by-layer nature of AM mandates a different approach to part design compared to traditional manufacturing processes. Ponche *et al.* have introduced a general methodology for DFAM in which they primarily focus on the orientation of the part, its geometry which is established using topological optimization, and the process conditions, such as the laser parameters, that need to be employed for the part [20]. According to Ponche *et al.*, part orientation refers to positioning the functional surfaces of a part being designed in such a way that it leads to the best surface finish and accuracy.

The part geometry can be potentially designed with the help of topological optimization, i.e., in a particular design space, for a given set of loads, boundary conditions and constraints, the material layout is optimized to achieve high performance of the system [20, 21]. Similarly, Kranz *et al.*, have recommended

design guidelines for laser additive manufacturing (LAM) by analyzing the effect of part orientation, size, and position on the dimensional accuracy and surface finish of lightweight parts, such as, thin-walls, bars [22]. The effect on surface quality of a part was studied by manufacturing parts with upward and downward facing surfaces which are built at various orientation angles with respect to the build platform. Kranz *et al.* observed that parts with the smallest angle have the lowest surface roughness; a low surface roughness is desirable.

To study the effect of part position in the powder bed on part accuracy, they designed test parts, which included a rectangular structure, a cylindrical structure, and a thin-wall structure, and placed this test part in five different locations on the powder bed, namely, middle, upper right, lower right, upper left, and lower left. It was concluded that the part position has no discernable effect on the accuracy of the test geometry for this particular experimental setup. To study the effect of orientation and size on part accuracy, parts with three different cross-sections, i.e., elliptical, cylindrical, and rectangular were chosen, and the aspect ratios (length-to-thickness ratio) of each part was varied. For thin-wall structures (rectangular cross-section), it is observed that to obtain good quality, the thickness should be greater than 0.4 mm, the orientation angle with reference to the build platform should be 90°, and the orientation angle in with reference to the re-coater device should be 45°. Lastly, the study on bore holes (cylindrical cross-section) shows that the highest part accuracy is obtained when it is built orthogonal to the build platform.

A detailed study on design rules was done by Daniel Thomas in his doctoral dissertation [23]. Thomas studied fundamental geometries, such as overhang features, which can then be used to design complex geometries. Through simple cuboidal builds, the author observed that orientation of the part (with respect to the build surface) plays an important role in the surface quality of the part. It is observed that surfaces built under an orientation angle (vertical inclination) of 45° to the build platform need support structures to avoid build failure. The optimum orientation angle to build surfaces is seen to be 90° to the build platform. The author suggests that the up-facing surfaces have poor surface quality under 45° orientation angle, but an abrupt improvement is seen when part is built at 0° angle to the build platform. To build geometries such as overhangs without support structures, the author suggests to use features which eschew the need for support structures, namely, chamfers, convex and concave radii. Thomas reports that chamfers can be built with orientation angle (with respect to the build plate) of more than 45°. The convex and concave radii need to be built at the varying bottom and top tangent angle of the radii to avoid the use of support structures, and these angles can be found in a tabulated format in Ref. [23]. To prevent surface merging while building parts such as, channels, slots, keyways etc., it necessary to have a minimum gap between features which is recommended to be 0.3 mm. Thomas' research conforms with the results obtained by Kranz et al., that the minimum thickness of thin-wall should be

0.4 mm [22, 23]. Subsequently, holes were also studied by Kranz *et al.* It is recommended that the minimum hole size should be 0.7 mm diameter when they are built parallel (self-supporting) to the build plate, and 1 mm when building perpendicular to the build plate.

Dunbar et al. conducted a quality assessment of Inconel 625 thinwalls made using LPBF [24]. To observe the effect of thin-wall angle with respect to the build plane (X-Y direction) on the thinwall quality, thin-walls were built at angles of 45°, 67.5° and 90°. Furthermore, to study the effect of re-coater blade motion on the quality of thin-walls, the orientation of thin-walls with reference to the re-coater blade direction was either 90° (perpendicular to re-coater), or 45° (rotated 45° along Z-axis). The thin-walls are built by varying the laser power, laser velocity, hatch pattern, and four thin-walls are built by using the parameter settings suggested by the manufacturer of the machine. It was observed with the help of a XCT scan analysis of the thin-walls that the thinnest thin-wall (median= 113 µm) with no porosity was built at a build angle (with reference to re-coater blade direction) of 45° (rotated 45° along Z-axis), laser power of 100 W, laser speed 900 mm/s, and thin-wall angle (with reference to build plane, X-Y direction) of 90°.

In a study by Adam *et al.*, design rules for two types of structures, namely, *element transitions*, and *aggregated structures*, were formulated [25]. According to the authors, combination of basic elements (e.g. cuboidal structure) are called element transitions (e.g., joints), and the arrangement of these element transitions along with multiple basic elements are called aggregated structures (e.g., overhangs). To study the effect of varying thickness and orientation on element transitions, a Y- shaped test specimen (Figure 4) was designed. This test specimen was built in three different orientations as seen in Figure 4, and the thickness (T_1, T_2, T_3) of the three elements are varied between 2 mm and 5 mm, namely, $T_1 = 2$ mm, $T_2 = 5$ mm, $T_3 = 5$ mm.

Adam et al., found no evidence that the aforementioned orientations affect the part quality. However, the thicknesses should be chosen so that the cross-sectional areas of element transitions in the build plane should remain the same size, or should reduce, to avoid surface defects, i.e., the cross-sectional areas of elements T_1 and T_2 should remain the same or be less in comparison to that of T_3 . Further, Adam et al. study the effect of edge morphology on part quality. It is concluded that to avoid defects, parts with sharp outer edges should be avoided, and similarly, parts should not have sharp inner edges for ease of removal of support structures and residual powder. Finally, for structures which have non-bonded elements, should have the following minimum gap (H_G) values for different AM process: laser sintering (SLS) ($H_G \ge 0.6 \text{ mm}$), laser melting (LPBF) $(H_G \ge 0.2 \text{ mm})$, fused filament fabrication (FFF) $(H_G \ge$ 0.4 mm) [25]. In the case of aggregated structures, namely, overhang, to ensure a robust manufacturability the authors suggest that the length of the overhang should be as follows:

laser melting ($L_{OH} \le 2.0$ mm), and fused filament fabrication ($L_{OH} \le 1.8$ mm).



Figure 4: Test specimen drawing adopted from Adam *et al.* [25]. Test specimen is built in three different orientations, namely, (a) depth of specimen along the X-Y axis, (b) height of the specimen along the Z-axis, and (c) height of the inverted specimen along the Z-axis of the build direction.

A summary of the design rules established from the above discussed works is given in the Appendix. Most of these pioneering works formulate design rules for AM based on measurements made with rudimentary instruments, such as, calipers, which do not capture the geometric and build integrity in a more detailed manner. In this thesis, we introduce design rules by analyzing data from X-ray computed tomography (XCT) scan, and layer-wise in-process images of the test specimen.

3 Experimental Studies and Data Acquisition

3.1 Test-artifact with thin-wall

For building the titanium alloy (Ti-6Al-4V) thin-wall test parts the following process parameters were used: laser power, P = 340 W; layer thickness, T = 60 µm; hatch spacing, H = 0.12 mm; and laser velocity, V = 1250 mm/s, resulting in the volumetric energy density $E_V = \frac{P}{H \times V \times T} = 37.8$ J/mm^3 . The parts were made using spherical ASTM B348 Grade 23 Ti-6Al-4V powder with a size distribution of 14 µm - 45 µm from LPW Technology, Inc.

Parts with the geometry exemplified in Figure 5 were built in three angular orientations to the re-coater blade with the dimension of 15 mm \times 15 mm \times 5.5 mm. Each part includes 25 thin-wall features whose thickness ranges from 0.06 mm to 0.3 mm, while the corresponding height increases from 0.6 mm to 3 mm. The length of each thin-wall is 11 mm, and they are built vertically upwards with 60 μ m layer thickness. The entire part was built in 90 layers [26].

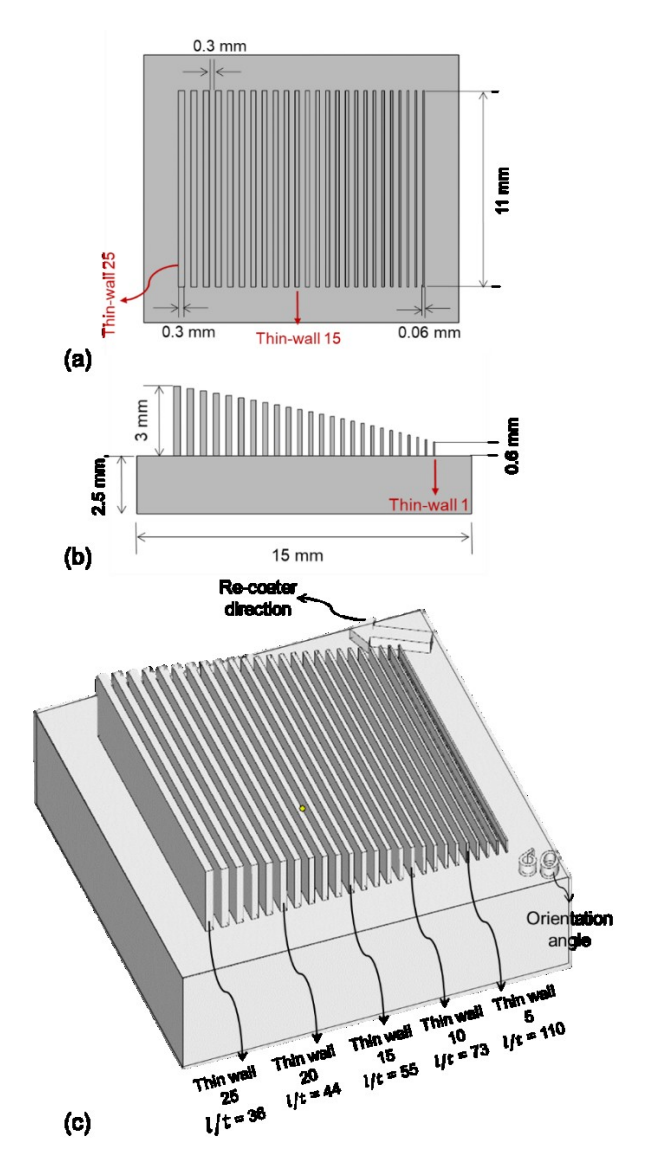


Figure 5: Computer aided design (CAD) of thin-walls in the test part. (a) Top view, (b) front view. (c) 3-D view of the test part at an orientation angle of 60° to the re-coater blade direction. In this work, two hatch patterns are used to build thin-wall structures as shown in Figure 9. The hatch pattern used to build thin-walls with aspect ratio (l/t) ranging from 36 to 157, i.e., thickness of 0.07 mm to 0.3 mm (thin-wall number 2 to 25) is shown Figure 9(a). This hatch pattern has an outer contour, inner contour, and hatches at the same angle inside the inner contour. The hatch pattern used to build thin-wall number 1 with aspect ratio (l/t) of 183, i.e., thickness of 0.06 mm is shown in Figure 9(b). Thinwall number 1 is built with an outer contour, hatches at the same angle, but without an inner contour.

3.2 Setup for in-situ process powder bed imaging

The in-situ process sensor data is acquired with the setup shown in Figure 6. The layer-wise images of the powder bed are captured using a digital single-lens reflex camera (DSLR, Nikon D800E) with an effective resolution of 36.3 megapixels which is mounted in a custom made enclosure inside the machine [27]. The flash lamps are located at three different locations in the machine (EOS M280) as shown in Figure 6, and they are used to capture five images of the powder bed at every layer in various lighting conditions (Figure 7).

These images are obtained after the laser scan and after the recoating process. In order to capture images at these particular instances during the build, a proximity sensor is employed in the machine. This proximity sensor tracks the motion of the recoater blade, and accordingly, captures the images. For this work, we have analyzed images post laser scan with the lighting condition as shown in Figure 7(a). The sample data acquired from the apparatus is shown in Figure 8.

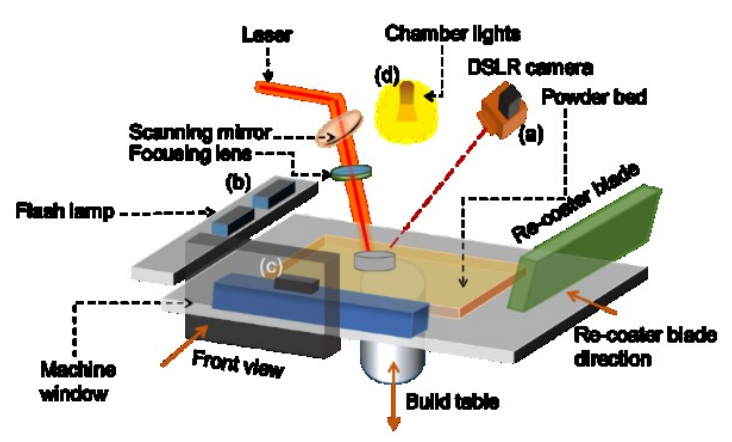


Figure 6: An illustration of the of the optical DSLR camera and flash lamps used for acquiring in-situ data [28].

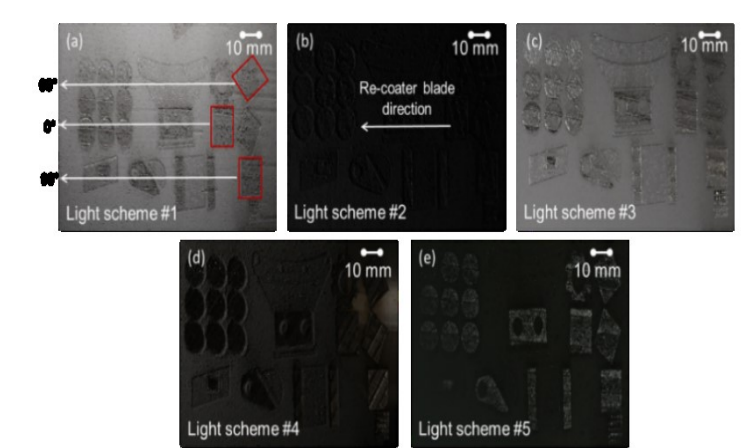


Figure 7: Powder bed images captured under different lighting schemes [28]. The different lighting schemes are obtained with the help of flash-lamps which are placed at various locations in the machine, as shown in Figure 6.

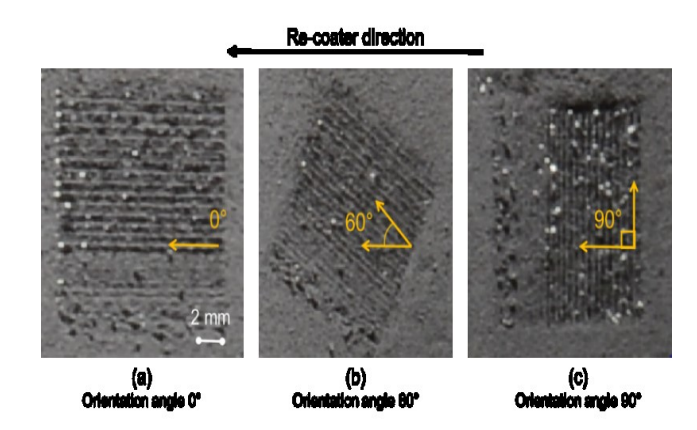


Figure 8: Optical images of a layer of thin-walls being manufactured at different orientation angles in the X-Y plane with respect to the re-coater blade direction, namely,(a)0°,(b) 60° , (c) 90° .

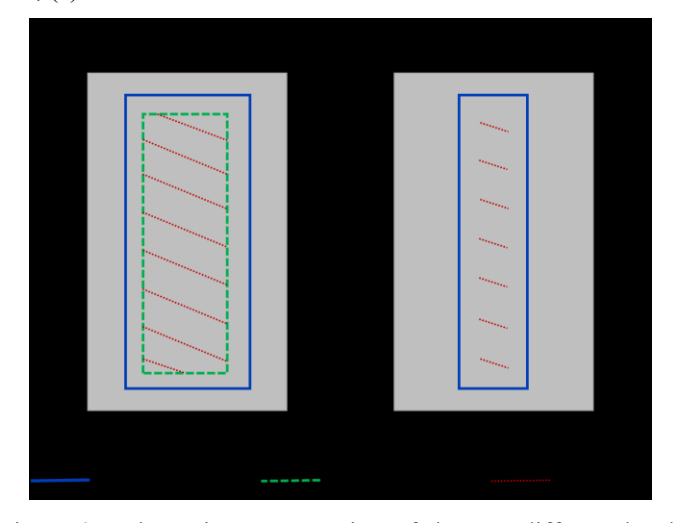


Figure 9: Schematic representation of the two different hatch patterns used to build thin-walls. (a) Hatch pattern used to build thin-walls with aspect ratio (l/t) ranging from 36 to 157, i.e., thickness of 0.07 mm to 0.3 mm (thin-wall number 2 to 25). (b) Hatch pattern used to build thin-wall number 1 with aspect ratio (l/t) of 183, i.e., thickness of 0.06 mm.

4 Research Methodology

This section is stratified into two sub-sections, wherein section 4.1 discusses the methodology applied to the offline XCT scan image data, and section 4.2 describes the convolutional neural network used to analyze the layer-wise in-situ powder bed images. The research approach is schematically reported in Figure 10.

Specifically, section. 4.1 has two phases, the first involves analysis of the XCT scan images of the thin-wall geometry (as seen in Figure 10), wherein certain quality-related features are extracted from the XCT scan images. These features are then combined in the form of Mahalanobis-squared distance which is used as a surrogate measure for tracking the build quality of the

thin-wall. The next phase is to predict the thin-wall quality from optical images. A convolutional neural network (CNN) is used for this purpose, in which the network is trained to predict the Mahalanobis-squared distance given in-situ process images of thin-wall boundaries. This type of neural network is referred to as a deep learning convolutional neural network because of the use of convolutional filters on different scales, which learn various aspects of the image from coarse to fine levels. The modalities of neural network are discussed in detail in section 4.2.

4.1 Offline Analysis of build quality using layer-wise XCT scan images

Firstly, the XCT scan of each test artifact is visually (qualitatively) examined layer-by-layer. The following inferences are rendered based on these visual observations. Figure 11 shows an example of layer number 18 under three different angular orientations.

- Thin-walls with thickness less than 0.1 mm, cannot be built irrespective of their orientation. The cause of this failure appears to be the overly thin cross-section of the thin-wall, which are too weak to resist the lateral force exerted by the re-coater.
- From the visual inspection of the zoomed in portion of a thin-wall with aspect ratio *l/t*= 44 (thickness= 0.25 mm)(Figure 11(b1), (b2) and (b3)), it is evident that the parts printed at orientation angle of 90° exhibit poor quality as compared to those printed in the other two orientation angles. The probable reason is that in the thin-walls built at 0° and 60° orientation angle (θ) the resistance offered by the thin-wall structure to the flow of the powder is less than that at 90°.

These observations are further examined and confirmed by analyzing the sliced images of the thin-wall XCT scans.

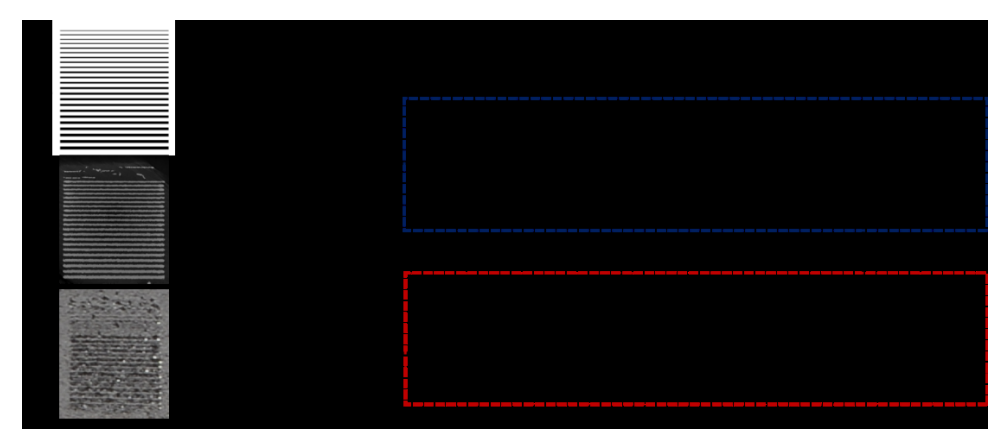


Figure 10: Outline of the methodology adopted to analyze XCT scan data with the help of CAD data for the thin-walls, and in-process powder bed images analysis.

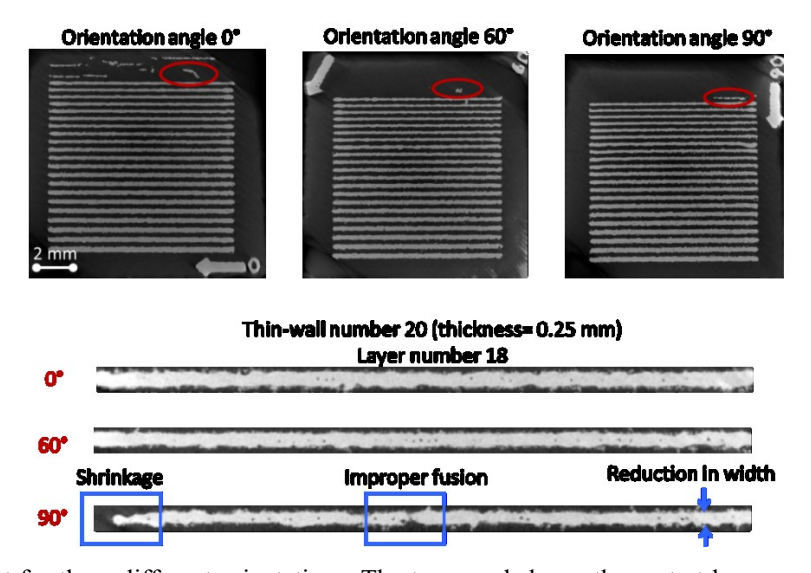


Figure 11: The thin-wall part for three different orientations. The top panel shows the part at layer number 18, and the bottom panel shows the individual thin-wall number 20 (l/t=44, thickness= 0.25 mm). The 90° orientation has the worst build quality.

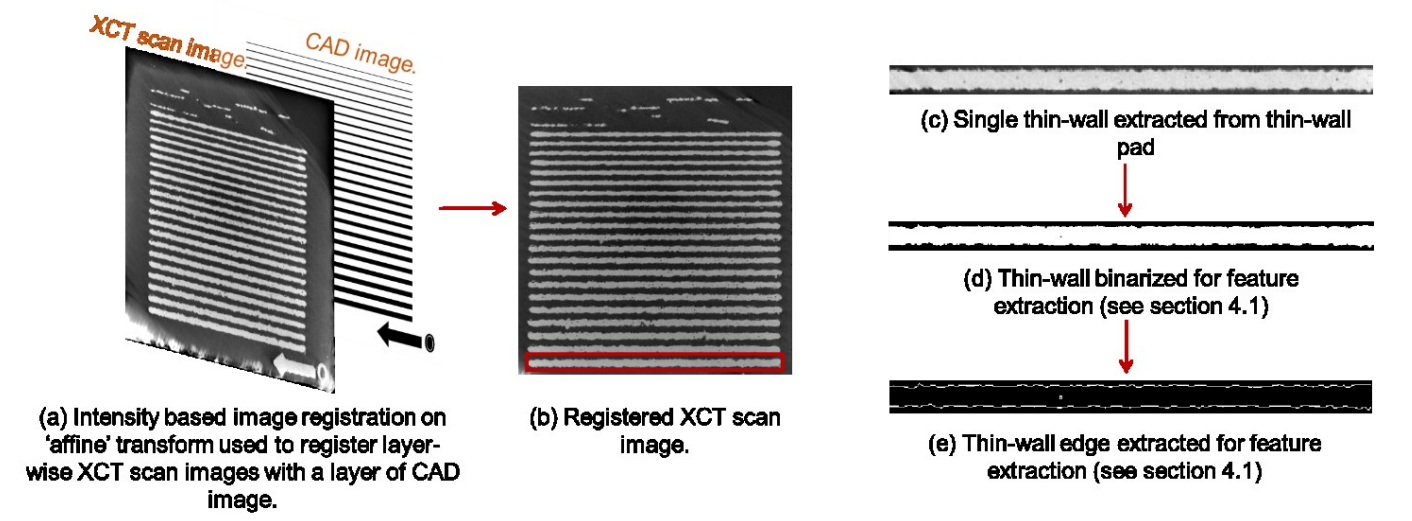
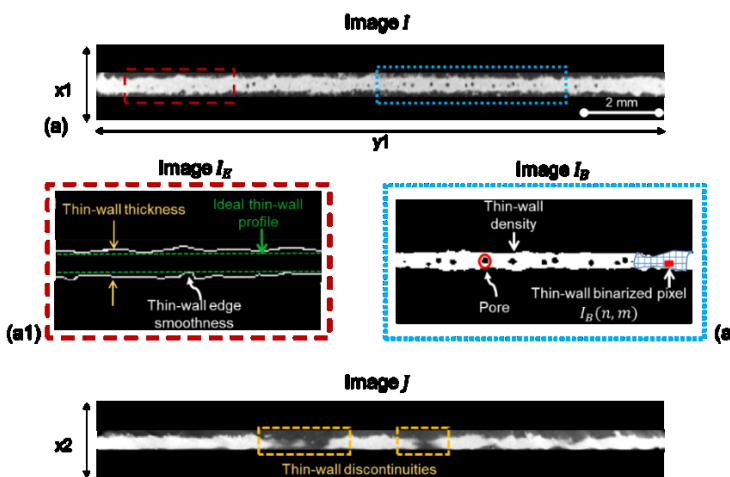


Figure 12:The extraction of thin-walls from XCT scan images. The thin-wall highlighted in (b) is extracted to as shown in (c). The -wall images shown in (d) and (e) are used for feature extraction.

At the outset, XCT scan for each thin-wall part is sliced with a layer thickness of 10 μ m, resulting in 300 images of each part. Subsequently, the CAD file for each test artifact is also sliced with an identical resolution of 10 μ m to register the CAD and XCT scan of layer-wise images.

Next, an intensity-based image registration approach is used to perform the affine transformation and align the XCT scan image to the corresponding CAD slice. Further, individual thin-walls are extracted from the registered images, and each thin-wall is further processed as depicted in Figure 12, to extract quantitative features as described shortly. The advantage of using these quantifiers is that they are based on two- dimensional image-based measurements, and involve simple matrix algebra, thus significantly reducing the computational burden involved for feature extraction.

A brief explanation regarding these features is provided herewith. Consider an XCT scan image I of a thin-wall of size x1 pixel \times y1 pixel (Figure 13(a)); the binarized segment of this image I is I_B (Figure 13 (a2)), and I_E is a segment that depicts the edge of the thin-wall, as shown in Figure 13 (a1)). The y1 dimension for the thin-wall image I, and y2 dimension of the thin-wall image I (Figure 13 (b)) are equal to 800 pixels and remain constant over all thin-wall images, i.e., if an image is considered to be a matrix with each pixel representing a matrix element, the number columns remains constant. On the contrary, the x1 and x2 dimensions for thin-wall image I and I, vary contingent to the thin-wall thickness, but it remains constant throughout all layers for a given thin-wall, for example, x1 = x2 = 36 pixels for thin-wall number 25, and x1 = x2 = 32 for thin-wall number 20.



y2

Figure 13: Thin-wall features extracted from XCT scan images. (a) Image I is a thin-wall extracted using methodology shown in Figure 12. Image I_E (a1) and Image I_B (a2) show three features extracted from the thin-walls, namely, thin-wall thickness, thin-wall edge smoothness, and thin-wall density. (b) Image I depicts the discontinuity in a thin-wall, which is used as the fourth feature.

Thin-wall thickness (\bar{t}) : This feature quantifies the average thickness of a thin-wall as follows. The edge of the thin-wall as shown in Figure 13(a1) and Figure 14, is obtained by applying a filter on the binarized image of thin-wall segment I_B . Further, the thickness of the thin-wall segment at a given location is determined by subtracting the first non-zero entry in a column of image pixel by the last entry in the same pixel column, as shown in Figure 14. This procedure estimates the distance between two edges of the thin-wall at a given location. The average of the distance between two edges of the thin-wall over the length (y1) is termed as the thickness of a thin-wall segment (\bar{t}) (Eqn. (1)).

$$\overline{t} = \frac{\sum_{i=1}^{m} \alpha_{1i} - \alpha_{2i}}{m}$$

where, α_{1i} = first non-zero row index, α_{2i} = second non-zero row index, m = number of columns.

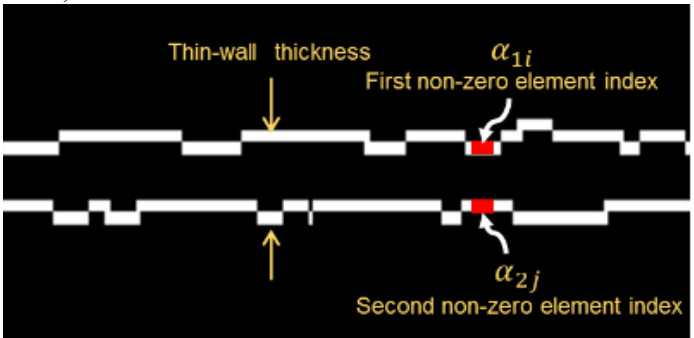


Figure 14: A representation of the thin-wall thickness feature. The pixels highlighted in red represent the pixels in the upper and lower edge of the thin-wall.

Thin-wall density (ρ_t): The thin-wall density quantifies unmelted or areas devoid of sufficient material that result in pores in an individual thin-wall (Figure 13 (a2)). To estimate this quantifier, the pixels within the boundary of the thin-wall image, is averaged to estimate ρ_t (Eqn. (2)).

$$\rho_{t} = \begin{cases} \frac{\sum_{i=1}^{m} \sum_{j=1}^{n} I(i,j)}{M} & for \ I > 0\\ 0 & for \ I < 0 \end{cases}$$
 (2)

where, I(i,j) is the pixel within the thin-wall, and M is the number of pixels within the boundary of a thin-wall image. In Figure 13 (a2), a pixel in a thin-wall image is shown.

Thin-wall edge smoothness (σ_s): This feature represents the degree of smoothness of the thin-wall XCT scan image boundary. The non-zero linear row indices of the upper edge (α_{1i}) and lower edge (α_{2i}) of the thin-wall, as shown in Figure 14, are recorded. The degree of smoothness of a thin-wall edge is evaluated by calculating the standard deviation of the column indices of each edge. This standard deviation is interpreted as follows: higher the standard deviation, lower will be the edge smoothness, and vice-versa.

The dotted-line in Figure 13 (a1) represents the edge of the thin-wall obtained from the computer-aided design (CAD) of the thin-wall. As observed visually, the CAD thin-wall edge has constant α_1 and α_2 values, and thus they have no standard deviation. Whereas, the thin-wall edges of the XCT scan images have highly varying values of edge indices, which results in high standard deviation, and in turn poor edge smoothness.

Thin-wall discontinuity (δ): The discontinuity of a thin-wall is highlighted in a yellow dotted-box in Figure 13 (b). If the thin-wall edge is discontinuous, it is likely to be porous, and it is more likely to fail in a structure application. It is defined as the number of instances (δ) that the non-zero row indices α_{1i} and α_{2i} (from

Eqn. (1))are not (1) tected in a thin-wall. A near-zero value of thin-wall segment discontinuity is preferred.

The above four quantifiers for each thin-wall XCT scan image are arranged in a matrix called the quantifier matrix (X^{θ}) , for each orientation $\theta = \{0^{\circ}, 60^{\circ}, 90^{\circ}\}\$ as shown in Figure 15. The quantifier matrix of each orientation angle is compared with features extracted from the CAD images of the thin-walls. The features extracted from the CAD thin-wall images are considered to be ideal, and hence, the features extracted from the XCT scan images are compared with them. The metric used for this comparison is known as the Mahalanobis-squared distance $((D_M^2)_i^{\theta})$ for orientation angle θ and thin-wall number $t = \{1, 2, 1\}$ 3...,25} as shown in Eqn. (3). Mahalanobis-squared distance is a metric used in multi-variate data analysis, i.e., data which has multiple variables in it. This distance accounts for the variability in the data due to multiple variables, and determines the degree of variability of each variable with the help of the inverse of the variance-covariance matrix which is also known as the precision matrix. In this work, we calculate the Mahalanobis-squared distance $((D_M^2)_i^{\theta})$ of a thin-wall with a particular aspect ratio (l/t) and orientation angle (θ) with respect to the corresponding CAD image of the thin-wall.

$$(D_M^2)_i^{\theta} = (\bar{X}_i^{\theta} - \mu^{TW})' S^{-1} (\bar{X}_i^{\theta} - \mu^{TW})$$

where, \bar{X}_i^{θ} is the feature vector of a particular thin-wall image i for orientation $\theta = \{0^{\circ}, 60^{\circ}, 90^{\circ}\}$ s which is to be compared with the thin-wall features extracted from a CAD image of the thin-wall. The features extracted from the CAD image are stored in μ^{TW} , and S^{-1} is the precision matrix (inverse of the covariance matrix) derived from the feature matrix of XCT scan images of a thin-wall with a particular orientation.

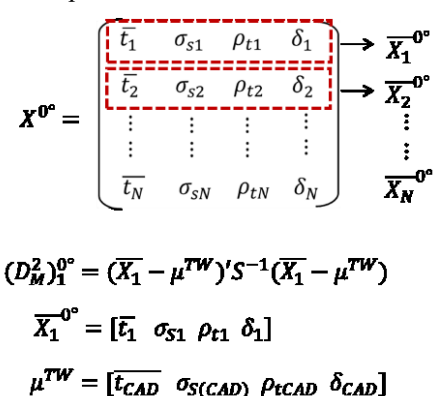


Figure 15: A representation of the arrangement of the quantifier matrix for a thin-wall at 0° orientation angle. $\overline{X_1}^{0^{\circ}}$ represents the features extracted from the first XCT scan thin-wall image with a particular aspect ratio and an orientation angle of 0° . μ^{TW} is the vector with features extracted from the CAD images of a thin-wall with a particular aspect ratio.

4.2 Online Analysis of in-process powder bed images

This section details the approach adopted to detect build failure in thin-walls by two-phase analysis of the in-process powder bed images: (1) the extraction of individual images of the thin-wall from the noisy powder bed images, and (2) predicting the quality of these images as inputs to a convolutional neural network (CNN) which is trained to predict the build quality of the thin-wall. We used an image filtering technique to sharpen the image and negate the noisy background as depicted in Figure 16. The resulting binary image has clearly demarcated edges for each of the thin-walls. This step is done with the help of linear filtering operation which is termed as convolution filter (not be confused with a CNN). Convolution is an operation in which the output pixel is the weighted sum of a set of neighborhood input pixels. The matrix of weights is called the convolution kernel, also known as the filter. Figure 16 shows the convolution kernel used in this case where, x is a variable which controls the intensity of sharpening of the image i.e. higher the value of x, the higher the erosion of the image.

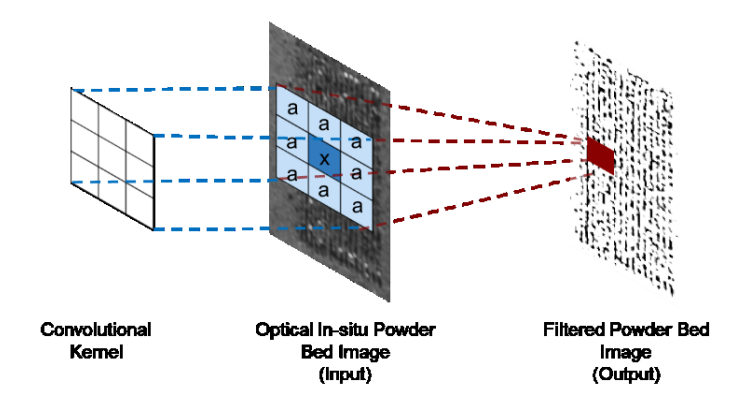


Figure 16: A schematic representation of image de-noising done by employing image sharpening. This technique uses a filter matrix which convolves around an image.

Convolutional neural network architecture

This section will briefly contrast the concept of the convolutional neural networks (CNN), vis-à-vis conventional feed-forward artificial neural networks (ANN) before providing mathematical details. ANNs are neurophysiologically inspired algorithms with neurons as their elementary units [29]. These neurons receive multiple inputs from either the input data or other neurons, later of the two being recurrent, and subsequently create an output by employing a non-linear transformation. The learning process to obtain the weights of the neurons is carried out using an algorithmic approach [30].

In a feed-forward ANN, neurons in a layer are fully connected, i.e., a neuron will be connected to all the neurons in the preceding

and succeeding layer, and are independent of each other. Due to this reason, ANNs are computationally expensive to implement back-propagation when analyzing high volume of data, and further, ANNs do not encapsulate the spatiotemporal correlation within the data, such as images.

For example, when analyzing an image of size 200×200×3, the resulting number of weights for the neurons in an ANN would be 200×200×3= 120,000. Furthermore, the large number of neurons will be required which will then lead to a large number of parameters, thus causing overfitting. In contrast in a CNN, a neuron in one layer will only be connected to a certain number of neurons in the previous layer, thus avoiding full-connectivity, and consequently, overfitting. Accordingly, CNNs are multilayered neural networks that have been used in detecting patterns from image pixels, such as, faces, hands, logos, text etc. [31, 32].

The CNN used in this work has four blocks along with a fully-connected layer, regression layer, input and output layer as seen in Figure 17. The input to the network is a binarized optical image of a single thin-wall in the size of 28×28 pixels which is extracted from de-noised layer-wise powder bed image, and the output is the corresponding Mahalanobis-squared distance of the thin-wall at the given layer. Each block has a 2D convolution layer with a rectified linear unit (ReLU), a batch normalization layer, and an average pooling layer.

Convolutional layer

The convolutional layer extracts features from an image by learning various convolving filters [33]. In this CNN architecture, we use an increasing number of filters in each convolutional layers to extract complex features from the images. A filter, is a $f \times f$ matrix, which convolves around an image and creates a feature map by performing a dot product operation on the input image, as shown in Figure 18. The manner in which the filter convolves over the input image is determined by a hyper-parameter called *stride*. Figure 18 (b1), is an illustration of a filter sliding over an image with stride set to 1. To preserve the dimensions of the images being convolved, the images are padded with zeros, i.e. the images are surrounded by zeros, before the convolution operation, and this hyper-parameter is called *padding*.

The convolutional neural network used in this work has four blocks, and each block has a convolutional layer in it, as shown in Figure 17. As the network gets deeper, the number of filters in each convolutional layer increases to extract high-level features from the image. This is represented in Figure 20 that the input image has a depth of 1 as it is a grayscale image, but the first convolution layer has depth of 8 filters. The depth of a layer is a function of the number of filters employed in a convolution layer, and the last convolution layer in block 4 has a depth of 32 filters.

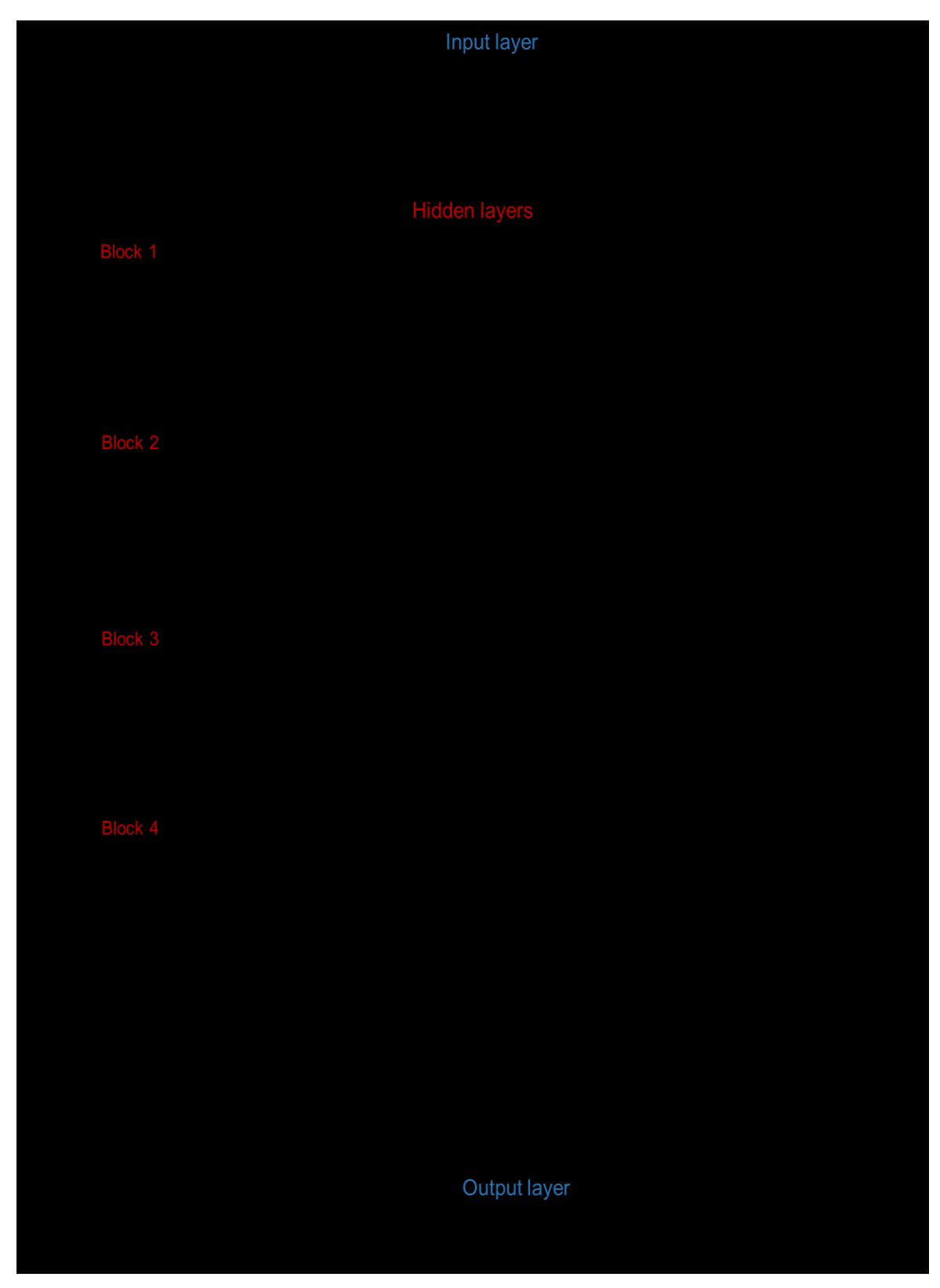


Figure 17: Flow-chart of the architecture of the convolutional neural network employed in this work to predict Mahalanobis-squared distance.

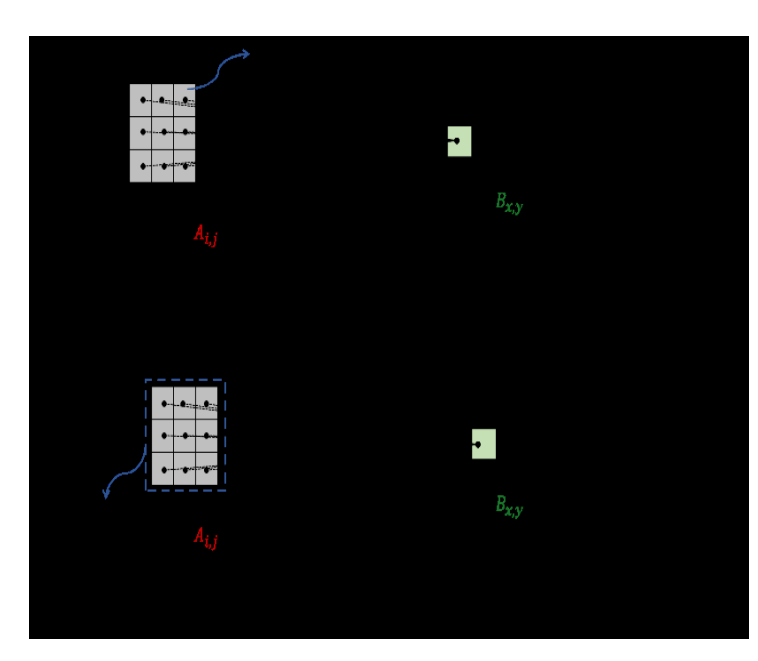


Figure 18: Schematic representation of convolution operation.

Batch normalization layer

The input given to a neural network is normalized, i.e. it has zero mean and unit variance, and this is done to quicken the learning process of the network. When the input variables of a network have extremely varying ranges, for example, one variable has a range of 1-1000, whereas the second one has a range of 1-2, the network parameters will have correspondingly wide range. This leads to a wide cost function in the direction of the variable with a wide range as it contributes more towards learning of the network. Due to this imbalance in the variables and the resulting elongated cost function, it becomes cumbersome to train a network. On the contrary, a neural network with normalized inputs has a circular cost function resulting in increased ease and speed of training. Likewise, it is advisable in deep neural network to normalize the input to every layer of the network, with the help of a technique called batch normalization [34].

When updating weights in one layer in a deep neural network, it is assumed that the layer's inputs will remain constant. However, the distribution of the input might change every time we update the weights, as the previous layer parameters are updated as well. In deep models, even small changes in earlier layers amplify drastically in the later layer, which significantly changes the input distribution to the later layers as well, making it hard for them to adapt to the changes, and thus, hindering convergence. This phenomenon is referred to as internal covariate shift, and batch normalization layers are employed in a deep neural network to prevent this phenomenon.

In batch normalization, the inputs are firstly normalized to zero mean and unit variance as shown below in Eqn. (4)-(6). This normalization is not performed on the whole input population at once, but is done on the input in batches [34].

$$\mu_B = \frac{1}{n} \sum_{k=1}^n a_k \tag{4}$$

$$\sigma_B^2 = \frac{1}{n} \sum_{k=1}^n (a_k - \mu_B)^2$$
 (5)

$$\widehat{a_k} = \frac{a_k - \mu_B}{\sqrt{\sigma_B^2}} \tag{6}$$

where, μ_B and σ_B^2 are the mean and variance of the batch respectively. $\widehat{a_k}$ is the normalized input value, and n is the batch size. Subsequently, the normalized inputs $(\widehat{a_k})$ are scaled and shifted to have an arbitrary mean and variance of the input distribution (Eqn. (7)).

$$o_k = \delta \widehat{a_k} + \alpha$$

where, o_k is an output of the batch normalization layer, and accordingly is the input to the activation (ReLU) layer. δ is the scaling factor, and α is the shifting factor, and these factors facilitate in randomizing the mean and variance of the batch inputs. Intuitively, it can be argued that these factors nullify the effect of normalization, as prior batch normalization, the data had random mean and variance. Taking a step backward, we can see that the mean and variance without batch normalization are dependent on excessively high number of parameter, such as, weights and biases of each neuron, activations etc., but in case of batch normalization they are dependent only on the two scaling and shifting factors which are trainable and learnable by the network.

When testing the network, the μ_B and σ_B^2 are not available, so the estimated of the population expectation and population variance are calculated as follows.

$$E_{k+1}[x] = \delta E_k[x] + (1 - \alpha) \mu_B$$
 (8)

$$Var_{k+1}[x] = \delta Var_{k}[x] + (1 - \alpha) \sigma_{R}^{2}$$
 (9)

In our neural network architecture used in this work, a batch normalization layer is employed in, as shown in Figure 17.

Rectified linear unit (ReLU) layer

The rectified linear unit (ReLU) is an activation function (non-linearity) which sets all negative values to zero [35]. It is formally given as follows.

$$f(x) = \begin{cases} x & \text{if } x \ge 0\\ 0 & \text{if } x < 0 \end{cases}$$
 (10)

The ReLU layers are preferred over other activation functions, such as the sigmoid function and the hyperbolic tangent (tanh) function, because it is found that the ReLU layers significantly accelerate the convergence of the stochastic gradient descent, i.e., the ability of the network to reach its cost/loss function minima [36]. Further, the ReLU layers are computationally inexpensive as they only involve thresholding of an activation matrix, whereas the sigmoid and tanh functions need heavy computations. Also, the ReLU layers avoid vanishing of the gradient which is quite evident in the hyperbolic tangent function

and sigmoid. Neural networks that are trained with the help of gradient-based learning method and back propagation method often encounter the vanishing-gradient problem [35].

These methods, provide the neurons with updated weights that are proportional to the partial derivative of the error function (the difference between the value predicted by the network and the actual value) with respect to the current weights of the neurons in each training iteration. When activation functions such as the tanh function and sigmoid function are used, the vanishing gradient problem is observed, as they have gradients in the range (0, 1), and backpropagation computes gradients by the chain rule. This results in the multiplication of n of these small numbers to compute gradients of the initial layers in an n-layer network, meaning that the gradient (error signal) decreases exponentially with n while the initial layers train very slowly. In other words, vanishingly small gradients prevent the training of the network as the weights remain constant after every iteration. In our network, we have used the ReLU layer in each block after the batch normalization layer as seen in Figure 17.

Average pooling layer

The average pooling layers are used to down-sample the spatial arrangement of an image (Figure 20) to reduce the computation, and also to avoid over-fitting, i.e., the network gets highly fitted to the training data, and cannot adapt to the inputs of the testing data, thus performing poorly. The spatial reduction is performed as it is sufficient to know the relative position of features with respect to other features, rather than knowing the exact feature location. Similar to a convolution layer, in an average pooling layer, filters of a given size move around an image in a nonoverlapping manner, resulting in a single value which is the average of all values of the image in the given filter size (Figure 19) [31]. Along with filter size, another hyper-parameter that the average pooling layer employs is stride, which dictates the movement of the filter over the image. The layer individually operates on each of the depth slice of the input image, thus conserving that dimension (Figure 20), and also the feature data accumulated from various filters.

In this work, we use average pooling layers in the first two blocks as seen in Figure 17. This layer is not used in the succeeding layers to avoid significant reduction in the spatial dimensions of the image resulting in feature data loss. The pooling layers use a filter size of 2×2 , and a stride of 2 in both blocks (Figure 19). This results in the reduction of input image size from 28×28 , to 7×7 at the end of the second block.

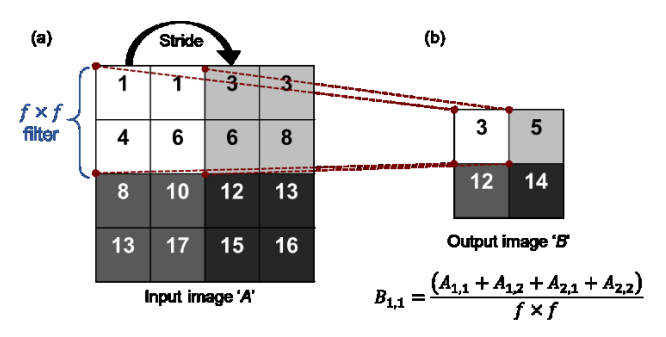


Figure 19: Schematic representation of an average pooling operation.

Fully connected layer

In a fully connected layer, all the neurons in the adjacent layers are pairwise connected to each other, but neurons in the same layers are independent of each other. Unlike a convolutional layer, the fully connected layer is a one-dimensional vector which has all activations of the previous layer, as seen in Figure 20. Due to this drastic change in dimension, fully—connected layers are placed at the end of the network, and convolution layers cannot be placed after them. Each convolution layer identifies features (e.g., lines, edges, curves, shapes) with the help of various filters, the fully-connected layer fuses these features together and come up with a prediction close to the desired output. The fully-connected layer in this network has 1568 inputs from the previous non-linearized (ReLU) convolution layer, and has a single output which is passed to the regression layer.

The mean-squared-error (MSE) is calculated between the predicted output and the desired output. In this regression layer, based on this MSE, weights of all neurons in the network are updated to obtain the optimum minima of the MSE. For training the network, values of hyper-parameters like maximum epochs (maximum number of iterations), and the learning rate for weights, were heuristically set to achieve the lowest value of MSE. The value of maximum epochs was chosen in such a way that it avoided under the network training, and also avoided overfitting. Similarly, learning rate of weights, which is a hyperparameter that controls the adjustment of the weights with respect to the cost function gradient, is set to an optimum level so as to preserve the network speed, and also not to miss out on a local minima of the cost function. For training the convolutional neural network, the input used is an individual thin-wall extracted from de-noised layer-wise powder bed images, and the output is the corresponding Mahalanobissquared distance of the fin obtained from the XCT scan image analysis. The data is allocated in the following manner: 75% for training the network, and 25% for testing the network. The data is randomly selected for training the network, and then the remaining data is used to test the network.

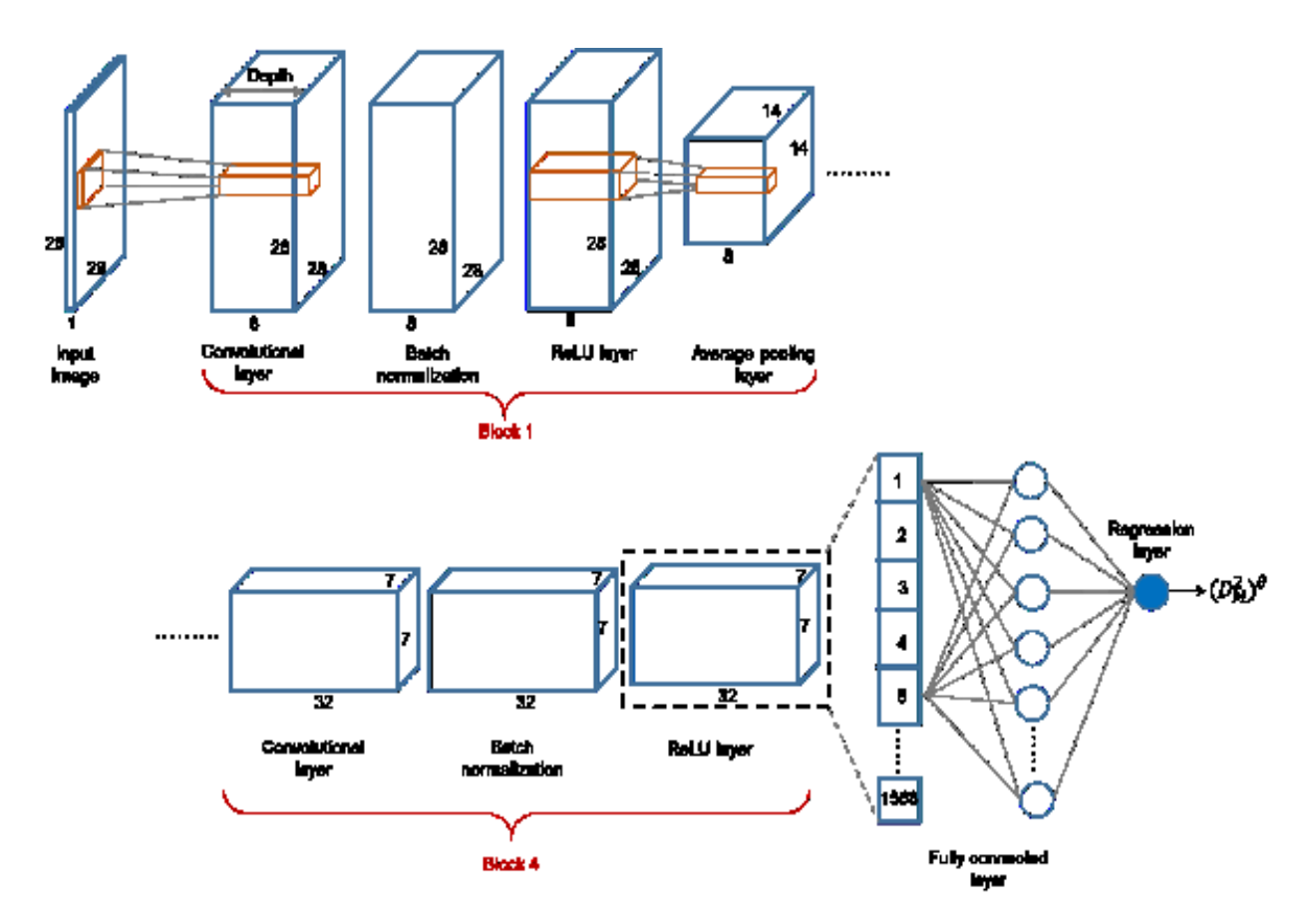


Figure 20: A schematic representation of the convolutional neural network architecture

5 Experimental Results

This section reports the results from the XCT scan image analysis described in section 4.1 in terms of the design rules for thin-wall structures, and in-process monitoring of thin-walls using the CNN described in section 4.2.

5.1 Design rules based on offline XCT scan images

In this section, we describe the results from analysis of the XCT slices, using the methodology described in section 4.1. The analysis leads to an understanding of the effect of orientation and aspect ratio of thin walls on the build quality of thin-wall structures.

For a fixed aspect ratio, the thin-walls oriented at 0° to the recoater direction, have a superior build quality. In other words, when the long edge of the thin-wall is parallel to the direction in which the re-coater moves, the thin-wall feature tends to build with fewer flaws, compared to those thin-wall structures that are built with the broadside of the thin-wall exposed to the re-coater. At an orientation of 90° , where the broadside of the thin-wall is perpendicular to the re-coater motion, the build quality is worst. However, the thin-wall built at orientation angle of 0° at layer number 22 is without any discernable flaws, see Figure 21 (a). Those built at 60° and 90° depict non-smooth edges and discontinuity. Furthermore, at layer number 25, irrespective of

the orientation angle have completely collapsed. In contrast, for a smaller aspect ratio, such as the thin-wall shown in Figure 21 (b), a discernable difference in the thin-wall quality at the three different orientations is seen only at layer 35. Here, the thin-wall built at 0°, as well as 60° have distinctly better geometric integrity, compared to the thin-wall built at 90°. An observation drawn from Figure 21 is that a threshold value of 15 can be arbitrarily set for the Mahalanobis-squared distance, beyond which the thin-wall quality is typically poor. We note that this observation is specific to particular work.

- a) Avoid building thin-walls below 0.15 mm thickness, i.e., aspect ratio (l/t) above 73, because they tend collapse.
- b) Avoid building thin-walls at angles inclined to the re-coater blade. In other words, avoid presenting the broadside of the thin-wall to the re-coater.
- c) The maximum recommended height for a thin-wall of thickness t is approximately $9 \times t$.

Next, we have summarized these results in terms of Figure 22, which maps the build height versus the aspect ratio averaged across all orientation angles, and recommended build height to achieve good geometrical integrity. The error bar in Figure 22(left) represents the standard deviation seen across all orientation angles for a given aspect ratio. Figure 22(right) depicts this information in greater detail with the recommended

height to build thin-walls with good geometrical integrity, and the height at which a thin-walls collapse with respect at a given orientation and aspect ratio. The design rules formulated from this work are summarized and pictorial represented in Figure 23.

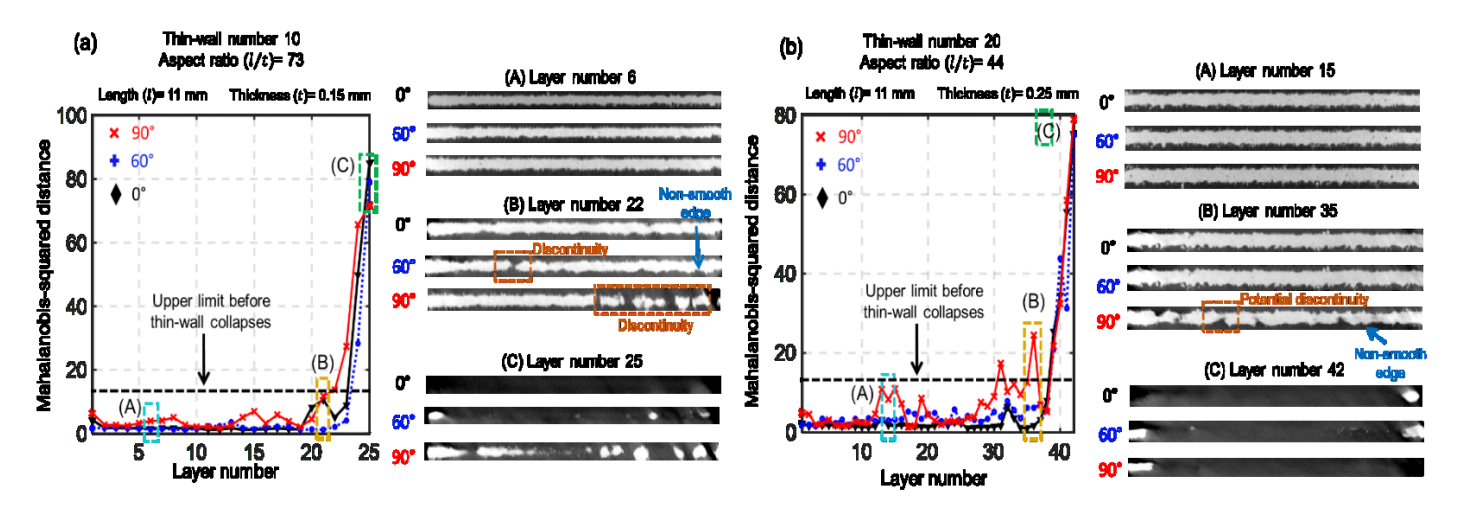


Figure 21: Mahalanobis-squared distance for different orientations (θ) of different thin-walls.(a) Thin-wall number 10, with aspect ratio (l/t) of 73, i.e., length l=11 mm and thickness t=0.15 mm. (b) Thin-wall number 20, with aspect ratio (l/t) of 44, i.e., length l=11 mm and thickness t=0.25 mm.

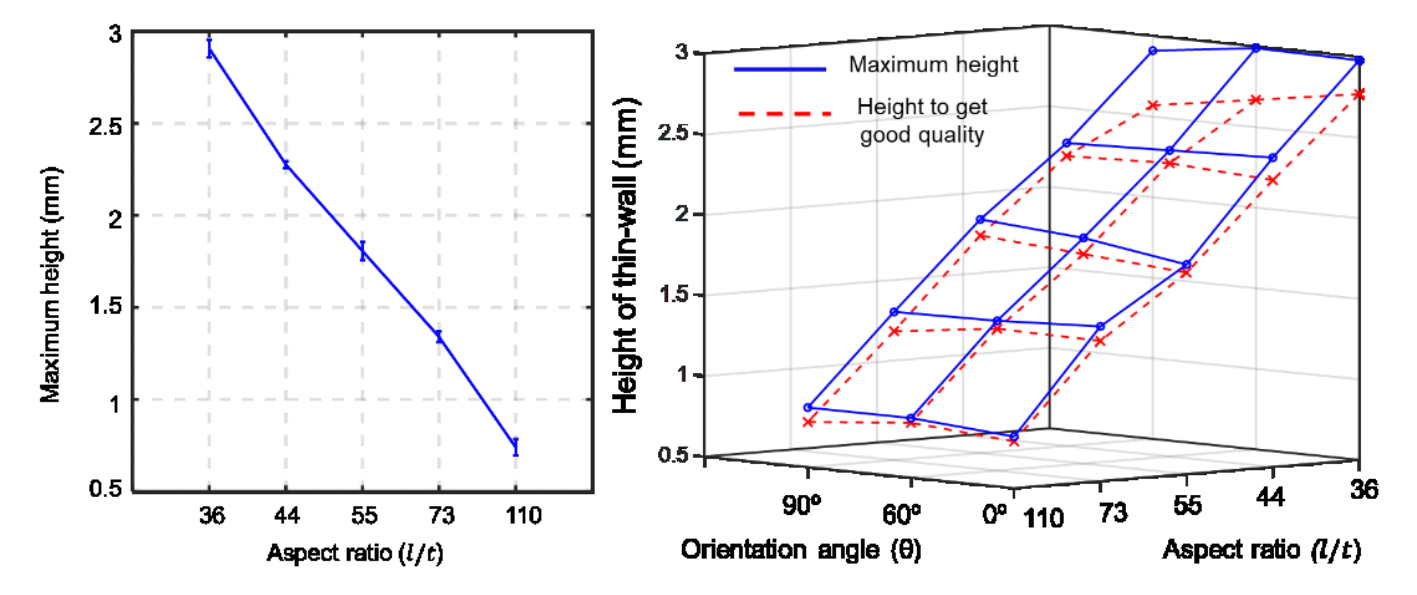


Figure 22: (left) Maximum recommended height to build thin-walls of good geometrical integrity with respect to aspect ratio (l/t). (right) Maximum build height of thin-walls to get good geometrical integrity, and height at which thin-walls collapse, with respect to aspect ratio and orientation angle.

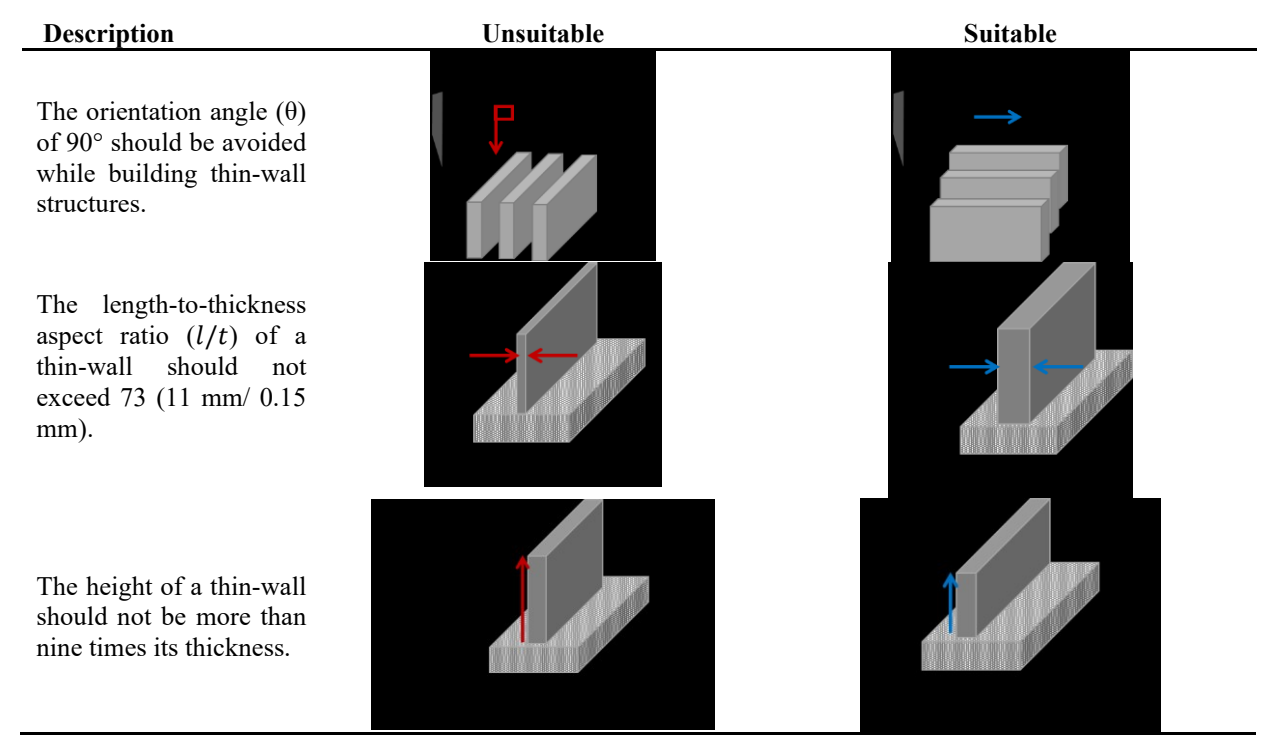


Figure 23: Summary and pictorial description of the design rules formulated from this work for thin-wall features built using metal laser powder bed fusion additive manufacturing process.

5.2 Results from in-process powder bed image analysis

In this section, we use the online layer-by-layer image data to detect the onset of defects in a thin-wall part. The key idea is to apply the convolutional neural network (CNN) described in section 4 to predict the Mahalanobis-squared distance as a surrogate or derived measure of build quality. The network training procedure and network architecture are explained in great detail in section 4.2. Figure 24 shows the representative results for thin-wall number 23 under three different

orientations. These results indicate that the CNN derived Mahalanobis-squared distance results, closely track those obtained using XCT scan image analysis of the thin-wall. As a consequence, instead of expensive post-process XCT scan measurements, the in-process image data can be used for detecting process defects in LPBF. As a quantitative measure to ascertain the closeness between the observed and CNN-predicted Mahalanobis-squared distance trends, we used the Pearson coefficient. For trends shown in Figure 24, the Pearson correlation coefficient ranges from 80% to 98%.

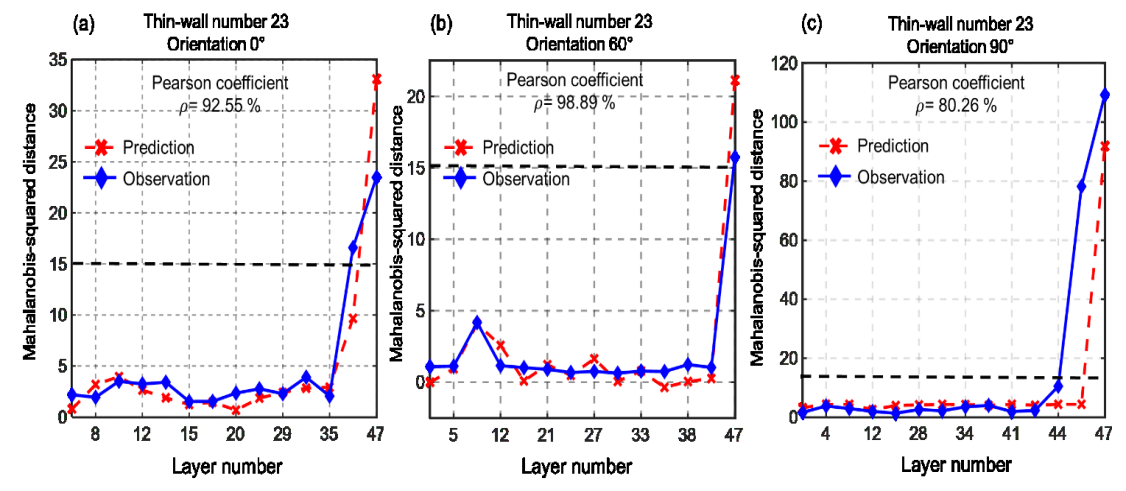


Figure 24: Mahalanobis-squared distance prediction via CNN regression for thin-wall number 23 (l/t=39, length= 11 mm, thickness= 0.28 mm) with (a) 0° orientation, (b) 60° orientation and (c) 90° orientation.

6 Conclusions and future work

This work investigated the quality of thin-wall parts made using the LPBF process as a function of their build orientation and aspect ratio (length-to-thickness ratio, l/t). Furthermore, inprocess optical image data of the powder bed was acquired to detect build flaws. Specific contributions from this work are as follows:

- 1) The effect of aspect ratio and wall thickness was quantified by extracting statistical features from the offline X-ray computed tomography (XCT) scan images of thin-wall parts. The following results are reported herein from the perspective of design of additive manufacturing (AM). The number of layers (vertical height) of a thin-wall part that can be built without damage is contingent on its aspect ratio (l/t ratio), and orientation to the recoater (θ). It is recommended that a thin-wall be built with 0° orientation with the re-coater blade. In other words, the broadside of the fin should not, as far as possible, face the re-coater direction. The maximum vertical height of the thin-wall should be less than 9 times of its thickness.
- 2) Four quantifiers were defined and extracted to characterize the geometric integrity of the thin-wall. These quantifiers were aggregated in terms of the Mahalanobis-squared distance, which were positively correlated with the visual quality of the thin-wall.
- 3) From the in-process quality monitoring vista, we trained a convolutional neural network (CNN) to predict the thin-wall quality (in terms of the Mahalanobis-squared distance) based on in-process optical images of the powder bed. For the representative cases tested, the Pearson correlation coefficient (ρ) between the Mahalanobis-squared distance measured from the XCT scan signatures, and the CNN derived Mahalanobis-squared distance was in the range of 80% to 98%.

This work thus makes a foray into deriving quantitative rules for optimal design of LPBF parts, specifically thin-wall structures. Furthermore, we have developed a feature-free deep learning approach to detect build flaws in LPBF parts. Consequently, this work makes an effort to complete the following link from the LPBF perspective: Part design \rightarrow In-process data \rightarrow Build quality. However, the following question remain to be addressed, which we will endeavor to answer in our future forays in the area:

- What is the generalizability of the design rules proposed to reduce variations in material and thin-wall structures for different process conditions such as, laser power and velocity?
- 2) How do the proposed design rules for thin-walls carry over to internal thin-wall features, and thin-wall with overhang geometries?
- 3) What is the ability of the CNN proposed in this work to apply to other types of features through transfer learning?

Acknowledgements

The experimental portion of this work was supported by the Air Force Research Laboratory through America makes under Agreement No. FA8650-12-2-7230. This work is supported in part by the National Science Foundation (NSF) Center for e-Design (Lockheed Martin) at Pennsylvania State University, and the NSF grant CMMI-16171488. We gratefully acknowledge the valuable contributions of the faculty, staff, and students at Penn State's Center for Innovative Materials Processing through Direct Digital Deposition (CIMP-3D) for providing the data utilized in this research. One of the authors (PKR) thanks the NSF for funding his work through CMMI-1752069 (CAREER) at University of Nebraska-Lincoln.

References

- [1] Yao, B., Imani, F., Sakpal, A. S., Reutzel, E., and Yang, H., 2018, "Multifractal analysis of image profiles for the characterization and detection of defects in additive manufacturing," Journal of Manufacturing Science and Engineering, 140(3), p. 031014
- [2] DebRoy, T., Wei, H., Zuback, J., Mukherjee, T., Elmer, J., Milewski, J., Beese, A., Wilson-Heid, A., De, A., and Zhang, W., 2017, "Additive manufacturing of metallic components—process, structure and properties," Progress in Materials Science
- [3] Sames, W. J., List, F. A., Pannala, S., Dehoff, R. R., and Babu, S. S., 2016, "The metallurgy and processing science of metal additive manufacturing," International Materials Reviews, 61(5), pp. 315-360.doi:10.1080/09506608.2015.1116649
- [4] Imani, F., Gaikwad, A., Montazeri, M., Rao, P., Yang, H., and Reutzel, E., 2018, "Process Mapping and In-Process Monitoring of Porosity in Laser Powder Bed Fusion Using Layerwise Optical Imaging," Journal of Manufacturing Science and Engineering, 140(10), pp. 101009-101009-101014.doi:10.1115/1.4040615
- [5] Frazier, W. E., 2014, "Metal Additive Manufacturing: A Review," Journal of Materials Engineering and Performance, 23(6), pp. 1917-1928.doi:10.1007/s11665-014-0958-z
- [6] Zwier, M. P., and Wits, W. W., 2016, "Design for additive manufacturing: Automated build orientation selection and optimization," Procedia CIRP, 55, pp. 128-133
- [7] Gao, W., Zhang, Y., Ramanujan, D., Ramani, K., Chen, Y., Williams, C. B., Wang, C. C., Shin, Y. C., Zhang, S., and Zavattieri, P. D., 2015, "The status, challenges, and future of additive manufacturing in engineering," Computer-Aided Design, 69, pp. 65-89
- [8] Grasso, M., and Colosimo, B. M., 2017, "Process defects and in situ monitoring methods in metal powder bed fusion: a review," Measurement Science and Technology, 28(4), p. 044005

- [9] Spears, T. G., and Gold, S. A., 2016, "In-process sensing in selective laser melting (SLM) additive manufacturing," Integrating Materials and Manufacturing Innovation, 5(1), p. 2.doi:10.1186/s40192-016-0045-4
- [10] Gong, H., 2013, "Generation and detection of defects in metallic parts fabricated by selective laser melting and electron beam melting and their effects on mechanical properties,"
- [11] Dunbar, A., Denlinger, E., Heigel, J., Michaleris, P., Guerrier, P., Martukanitz, R., and Simpson, T., 2016, "Development of experimental method for in situ distortion and temperature measurements during the laser powder bed fusion additive manufacturing process," Additive Manufacturing, 12, pp. 25-30
- [12] Dunbar, A. J., Denlinger, E. R., Gouge, M. F., Simpson, T. W., and Michaleris, P., 2017, "Comparisons of laser powder bed fusion additive manufacturing builds through experimental in situ distortion and temperature measurements," Additive Manufacturing, 15, pp. 57-65.doi:https://doi.org/10.1016/j.addma.2017.03.003
- [13] Scime, L., and Beuth, J., 2018, "Anomaly detection and classification in a laser powder bed additive manufacturing process using a trained computer vision algorithm," Additive Manufacturing, 19, pp. 114-126
- [14] Scime, L., and Beuth, J., 2018, "A multi-scale convolutional neural network for autonomous anomaly detection and classification in a laser powder bed fusion additive manufacturing process," Additive Manufacturing, 24, pp. 273-286
- [15] Yao, B., and Yang, H., 2018, "Constrained Markov Decision Process Modeling for Sequential Optimization of Additive Manufacturing Build Quality," IEEE Access
- [16] Yao, B., Imani, F., and Yang, H., 2018, "Markov Decision Process for Image-guided Additive Manufacturing," IEEE Robotics and Automation Letters
- [17] Hague *, R., Mansour, S., and Saleh, N., 2004, "Material and design considerations for rapid manufacturing," International Journal of Production Research, 42(22), pp. 4691-4708.doi:10.1080/00207840410001733940
- [18] Rosen, D. W., 2014, "Research supporting principles for design for additive manufacturing," Virtual and Physical Prototyping, 9(4), pp. 225-232.doi:10.1080/17452759.2014.951530
- [19] Atzeni, E., and Salmi, A., 2012, "Economics of additive manufacturing for end-usable metal parts," The International Journal of Advanced Manufacturing Technology, 62(9), pp. 1147-1155.doi:10.1007/s00170-011-3878-1
- [20] Ponche, R., Kerbrat, O., Mognol, P., and Hascoet, J.-Y., 2014, "A novel methodology of design for Additive Manufacturing applied to Additive Laser Manufacturing

- process," Robotics and Computer-Integrated Manufacturing, 30(4), pp. 389-398
- [21] Bendsoe, M., and Sigmund, O., 2004, "Topology Optimization: Theory, Methods, and Applications ".doi:10.1007/978-3-662-05086-6
- [22] Kranz, J., Herzog, D., and Emmelmann, C., 2015, "Design guidelines for laser additive manufacturing of lightweight structures in TiAl6V4," Journal of Laser Applications, 27(S1), p. S14001
- [23] Thomas, D., 2009, "The development of design rules for selective laser melting," Ph.D. Dissertation, University of Wales.
- [24] Dunbar, A. J., Gunderman, G. J., Mader, M. C., and Reutzel, E. W., 2017, "Fabrication and Quality Assessment of Thin Fins Built Using Metal Powder Bed Fusion Additve Manufacturing," Solid Freeform Fabrication Symposium An Additve Manufacturing ConferenceAustin, Texas, USA, p. 2650.
- [25] Adam, G. A. O., and Zimmer, D., 2014, "Design for Additive Manufacturing—Element transitions and aggregated structures," CIRP Journal of Manufacturing Science and Technology, 7(1), pp. 20-28.doi:https://doi.org/10.1016/j.cirpj.2013.10.001
- [26] Chen, R., Imani, F., Reutzel, E. W., and Yang, H., 2018, From Design Complexity to Build Quality in Additive Manufacturing A Sensor-based Perspective.
- [27] Abdelrahman, M., Reutzel, E. W., Nassar, A. R., and Starr, T. L., 2017, "Flaw detection in powder bed fusion using optical imaging," Additive Manufacturing, 15, pp. 1-11.doi:https://doi.org/10.1016/j.addma.2017.02.001
- [28] Imani, F., Gaikwad, A., Montazeri, M., and Rao, P., 2018, "Layerwise In-Process Quality Monitoring in Laser Powder Bed Fusion," ASME, Manufacturing Science and Engineering Conference Texas A&M.
- [29] Hagan, M. T., Demuth, H. B., and Beale, M., 1997, Neural Network Design, PWS Publishing, Boston, MA.
- [30] Williams, J., Dryburgh, P., Clare, A., Rao, P., and Samal, A., 2018, "Defect Detection and Monitoring in Metal Additive Manufactured Parts through Deep Learning of Spatially Resolved Acoustic Spectroscopy Signals,"
- [31] LeCun, Y., Kavukcuoglu, K., and Farabet, C., 2010, "Convolutional networks and applications in vision," ISCAS, pp. 253-256
- [32] Zhang, X., Zhao, J., and LeCun, Y., 2015, "Character-level convolutional networks for text classification," Advances in neural information processing systems, pp. 649-657
- [33] LeCun, Y., and Bengio, Y., 1995, "Convolutional networks for images, speech, and time series," The handbook of brain theory and neural networks, 3361(10), p. 1995

- [34] Ioffe, S., and Sezegdy, C., 2015, "Batch Normalization: Accelerating Deep Network Training by Reducing Internal Covariate Shift," CoRR, abs/1502.03167
- [35] Glorot, X., Bordes, A., and Bengio, Y., 2011, "Deep Sparse Rectifier Neural Networks," Proceedings of the Fourteenth International Conference on Artificial Intelligence and Statistics,
- G. Geoffrey, D. David, and D. Miroslav, eds., PMLR, Proceedings of Machine Learning Research, pp. 315--323.
- [36] Bottou, L., 1991, "Stochastic gradient learning in neural networks," Proceedings of Neuro-Nimes, 91(8), p. 12

Appendix

This table summarizes the design rules that were discussed in section 2.

| Ref. | Description | Unsuitable | Suitable |
|------------------|--|-----------------------------------|----------|
| Adam et al. [25] | The thickness of element transitions' (explained in section 2.1) should be such that the cross-sectional area in the building plane remains constant or reduces. | A_1 A_2 $A_3 > A_1 + A_2$ | |
| | To obtain good outer edge morphology, smooth edges should be used instead of sharp edges. | | |
| | To remove support structures with ease, inner edges should be rounded. | Sharp inner-edge Support material | |
| | Minimum gap between two consecutive features should be more than 0.2 mm. | | |

| Ref. | Description | Unsuitable | Suitable |
|--------------------------|--|---|-----------------------|
| Thomas [23] | Thin-wall structures should have thickness greater than 0.4 mm | Thickness: <0.4 nm | Thickness: > 0.4 from |
| | The gap between consecutive features should be more than 0.3 mm. | | |
| | To build overhang geometries chamfers above the orientation angle of 45° with respect to the build platform should be used as support structures. | Chantler angle 45° | |
| | Surfaces should be built vertical, i.e. orientation angle of 90° to the build platform to get good surface finish. | 45" (down-facing) S0" (vertical) | |
| Kranz <i>et al.</i> [22] | Thin-wall structures should be built at an orientation angle of 90° with reference to the build platform, and 45° with reference to the re-coater blade direction to get good quality build. | Fo control direction ASS 2 Y ASS 2 Built platform | |
| | Similar to Daniel Thomas, Kranz et al suggest that the thin-wall thickness should be more than 0.4 mm. | | Thickness: > 0.4 mm |
| | Through bore holes should be preferred over blind holes. The bore diameter should exceed 2 mm for well-defined holes. | | |